Chemical Engineering Journal 490 (2024) 151802

Contents lists available at ScienceDirect

Chemical Engineering Journal

journal homepage: www.elsevier.com/locate/cej

Boosting persulfate activation through efficient π → π* transition activated by Cu ion anchored porphyrin-based metal–organic framework

Wen-Qiang Li [a,b], Oleksandr Savateev [c], Yuan-Ming Li [d], Jian-Kang Zheng [b], Yi-Xuan Wang [b], Nannan Hou [b,*], Xiao-Cheng Liu [b], Rong-Rong Ding [b], Xiao-Guo Zhou [d], Yang Wang [b,c,*], Xian-Yang Shi [a,*], Yang Mu [b]

[a] School of Resources and Environmental Engineering, Anhui University, Hefei 230601, China
[b] CAS Key Laboratory of Urban Pollutant Conversion, Department of Environmental Science and Engineering, University of Science and Technology of China, Hefei 230026, China
[c] Department of Colloid Chemistry, Max Planck Institute of Colloids and Interfaces, Potsdam 14476, Germany
[d] Department of Chemical Physics, University of Science and Technology of China, Hefei 230026, China

ARTICLE INFO

Keywords:
Photocatalytic persulfate activation
Porphyrin-based metal organic frameworks
Electron transition
Cu ion
π-electron delocalization

ABSTRACT

Photocatalytic persulfate activation provides a promising approach for the elimination of persistent organic pollutants from water. This has been exemplified in porphyrin-based metal organic frameworks (PMOFs), which however come with ineffective electron transition within the porphyrin ligand. Herein, we present a Cu ion modification strategy capable of boosting electron transition by inducing electron delocalization under visible light. The introduction of Cu ions increased the degradation rate constant of ciprofloxacin (CIP) by nearly 44 times, surpassing most state-of-the-art photocatalysts. The in-situ characterizations and theoretical calculations suggest that π-electron localization constitutes the origin of ineffective electron transition in PMOFs. The introduction of Cu ions induces π-electron delocalization to intensify the π → π* transition, forming electron-rich centers of Cu to lower the energy barrier for O-O bond cleavage. This work offers fundamental insights into the electron transition within PMOFs, upon which the universal strategy is proposed for improved water decontamination performance via persulfate activation.

1. Introduction

Advanced oxidation processes (AOP) based on persulfate activation allow the continuous production of reactive oxygen species (ROS) with high oxidation potentials (*e.g.* $SO_4^{\bullet-}$: 2.6–3.1 V, $^{\bullet}OH$: 1.8–2.7 V), outperforming other counterparts (*e.g.* $Cl^{\bullet}$: 2.5 V, $Br^{\bullet}$: 2.0 V) for degradation of refractory pollutants from water [1–4]. Specifically, the low-cost and safe peroxydisulfate (PDS) has been extensively applied as feedstock to produce the ROS following appropriate activation pathways [5]. Among these, visible-light-enabled activation seems plausible for affording ROS in an energy-saving and sustainable fashion [6,7]. Similar to other solar-to-chemical conversion systems [8–11], photocatalytic PDS activation necessitates the participation of abundant photoelectrons to allow the rate-limiting O-O bond cleavage by lowering the energy barrier for producing ROS (Eqs. 1–2) [10,12]. In this regard, the development of the photocatalysts with superior performance is at the core to properly fit the purpose

$$\text{Photocatalyst} + h\nu \rightarrow \text{Photocatalyst}\,(e^-, h^+) \quad (1)$$

$$e^- + S_2O_8^{2-} \rightarrow SO_4^{\bullet-} + SO_4^{2-} \quad (2)$$

Metal-organic frameworks (MOFs), featuring well-defined molecular building blocks, supply a perfect platform for the design of high-performance photocatalysts because of flexible structural designability and functional modifiability [13,14]. Normally, MOFs are constituted by metal ions or clusters coordinated with organic ligands, where the ligands inside MOFs are often regarded as photosensitive motifs [15,16]. Porphyrin-based MOFs (PMOFs) have been demonstrated to possess excellent performance toward visible-light absorption, which is related to the porphyrin ligand molecules with intrinsically planar π-conjugated structure [17,18]. It is however noticed that the photocatalytic performance of PMOFs is largely hampered by the inefficient charge

* Corresponding authors at: CAS Key Laboratory of Urban Pollutant Conversion, Department of Environmental Science and Engineering, University of Science and Technology of China, Hefei 230026, China (Y. Wang).
E-mail addresses: hounan@ustc.edu.cn (N. Hou), ywangese@ustc.edu.cn, Yang.Wang@mpikg.mpg.de (Y. Wang), shixi381@163.com (X.-Y. Shi).

https://doi.org/10.1016/j.cej.2024.151802
Received 22 February 2024; Received in revised form 25 April 2024; Accepted 29 April 2024
Available online 1 May 2024

separation at the ligand site [19–21]. Combining the active metal–oxygen (*e.g.* iron-oxygen) cluster with the porphyrin ligand to initiate ligand-cluster charge transfer (LCCT) excitation appears to be promising to address this issue [22–24]. Nonetheless, the LCCT pathway requires mutually matched molecular orbital energy levels between the ligand and the cluster in PMOFs, which only come with limited success [22,25].

Alternative strategy taking advantage of independent charge separation at porphyrin ligands with intrinsically planar π-conjugated structure, should become feasible if the inherent electron transitions, such as $\pi \rightarrow \pi^*$ transition, are activated. Proper photoexcitation of the lone-pair electrons of N atoms in porphyrin could provide additional opportunities to intensify charge separation. Rational design at molecular level to tune the symmetric and planar π-conjugated framework remains largely unexplored. Recently, the new insights from carbon nitride (C_3N_4) display the encouraging excitation behavior upon forming the charge transfer channels by introducing transition-metal species into the π-conjugated structure [10,26–29]. It is therefore envisioned that doping of transition-metal species may intensify the electronic transition at the porphyrin ligand. This could lead to excellent photogenerated electron utilization of PMOFs, allowing otherwise high-energy-barrier bond cleavage in photocatalytic reactions. [10,30,31].

Herein, aluminum-based PMOF formulated as H_2TCPP $[AlOH]_2(DMF_3(H_2O)_2)$ (abbreviated as TCPP-Al, where TCPP stand for tetrakis(4-carboxyphenyl) porphyrin) was employed as an example, copper-doped TCPP-Al (termed as Cu@TCPP-Al) was further configured for proof-of-concept demonstration [32]. The coordination environment, microstructure, and optical properties of Cu@TCPP-Al were investigated using various characterization techniques. Then, we comprehensively evaluated the photocatalytic performance of Cu@TCPP-Al for PDS activation towards the degradation of a model pollutant (ciprofloxacin) bearing an electron-withdrawing group. Afterwards, the dominant ROS in the catalytic system were identified using radical quenching experiments and electron paramagnetic resonance (EPR) spectroscopy. The investigation was facilitated by in-situ characterizations and density functional theory (DFT), which allowed us to unravel the electron transition pathways in the π-conjugated structure of the ligand TCPP. This further clarified the impact of Cu species in terms of PDS activation.

2. Experimental procedure

2.1. Chemicals

All chemicals and agents were analytical grade, and used without purification unless otherwise specified. Aluminum chloride hexahydrate ($AlCl_3{\cdot}6H_2O$, AR), anhydrous copper acetate ($Cu(CH_3COO)_2$, AR), PDS ($Na_2S_2O_8$, AR), sodium hydroxide (NaOH, AR), ethanol (AR), N, N-Dimethylformamide (DMF, anhydrous, AR), and hydrochloric acid (HCl, 37 %) were purchased from Sinopharm Chemical Reagents, China. Ciprofloxacin (CIP, $C_{17}H_{18}FN_3O_3$, ≥98 %) was obtained from Shanghai Aladdin Biochemical Tech. Co., Ltd., TCPP molecule was prepared following established procedures [33]. Deionized water (R = 18.25 MΩ) was used in all the experiments.

2.2. Preparation of Cu@TCPP-Al

The pristine TCPP-Al was prepared via a simple solvothermal synthetic route with modifications [7]. Typically, 150 mg of $AlCl_3{\cdot}6H_2O$ and 200 mg TCPP were fully dissolved in 20 mL deionized water, which was then loaded into a Teflon-lined autoclave and kept at 180 °C for 24 h. After cooling down to room temperature, the dark purple crystals were collected by centrifugation at 11500 rpm for 10 min, followed by washing with DMF and deionized water for three times, respectively. Finally, Al-TCPP was obtained after drying at 80 °C overnight under dynamic vacuum.

Cu@TCPP-Al was synthesized from Al-TCPP *via* a post-processing step [34]. In detail, Al-TCPP was first activated overnight in dynamic vacuum at 170 °C. Next, the activated Al-TCPP was transferred into 5 mL of DMF solution containing 36.4 mg of anhydrous copper acetate, followed by reacting at 100 °C for 48 h. The resultant brick-red solid Cu@TCPP-Al was obtained via centrifugation at 11500 rpm for 10 min, followed by sequentially washing with DMF, deionized water and acetone, and finally dried at 60 °C.

2.3. Characterizations

The fundamental characterizations in more details are provided in supporting information (SI), including X-ray absorption near-edge spectroscopy (XANES), extended X-ray absorption fine structure (EXAFS, Cu K-edge), aberration-corrected high-angle annular dark-field scanning transmission electron microscopy (HAADF-STEM), field-emission transmission electron microscopy (FETEM), powder X-ray diffraction (PXRD) patterns and X-ray photoelectron spectroscopy (XPS) spectra, *etc*.

2.4. Pollutant degradation experiments

The CIP degradation experiments were performed at room temperature utilizing a 300 W xenon lamp system equipped with 420 nm filter. In detail, 4.0 mg of photocatalyst (80 mg/L) was homogeneously dispersed in 50 mL of 10 mg/L CIP solution. The initial pH of suspension was set to 7.02 using 0.1 M NaOH and HCl, followed by the addition of 12 mg of PDS (1 mM). The mixture was stirred in the dark for 30 min to reach the adsorption–desorption equilibrium. The photocatalytic experiment was then conducted at 25 °C. At different time intervals, 1.5 mL of suspension was gathered and centrifuged at 15,000 rpm for 2 min to gain the supernatant. The photocatalyst was collected by centrifugation at the end of each experiment, and then washed and dried for cyclic test and stability evaluation.

2.5. Calculation methodology

Using the commercially available program Materials Studio 2017 R2 [35], the TCPP-Al and X@TCPP-Al (X = Fe, Co, Ni, and Cu) models were created in order to screen out the metal with optimum binding affinity to TCPP-Al and to investigate the origin of the ineffective $\pi \rightarrow \pi^*$ transition within TCPP-Al. Geometry optimization of the models, distribution of partial density of states (PDOS), differential charge density and electron localization function (ELF) calculations were implemented using the CASTEP module [36]. The standard XRD patterns of the TCPP-Al and Cu@TCPP-Al models were obtained by performing Reflex module calculations on the geometrically optimized configuration. In particular, the Perdew-Burke-Ernzerhof (PBE) exchange correlation generalization function in the generalized gradient approximation (GGA) was employed to describe the electron interactions, while the interactions between the valence electrons and ion core were simulated by the projection enhanced wave (PAW) method [37]. The specific parameters were as follows: the cut-off energy was set to 440 eV; the computational accuracy of the electron self-association process was set to 2×10^{-6} eV $atom^{-1}$; and the sampling type of the Brillouin zone was Gamma point [38]. In addition, the different ion binding energies ΔE were calculated using Eq. (3) as follows [21,39].

$$\Delta E = E_{X@TCPP-Al} - E_{TCPP-Al} - E_X \quad (3)$$

where $E_{X@TCPP-Al}$, $E_{TCPP-Al}$ and E_X represent the total energy of TCPP-Al after doping with X ion, the energy of TCPP-Al and the energy of X ion, respectively.

The adsorption energy of PDS molecules (E_{ads}) at the TCPP-Al or Cu@TCPP-Al interface was calculated by the following Eq. (4)

$$E_{ads} = E_{PDS-Slab} - E_{Slab} - E_{PDS} \quad (4)$$

where $E_{PDS-Slab}$, E_{Slab} and E_{PDS} represent the total energy of TCPP-Al or Cu@TCPP-Al after adsorption of PDS, the energy of TCPP-Al or Cu@TCPP-Al, and the energy of PDS, respectively.

3. Results and discussion

3.1. Synthesis and structural characterizations of Cu@TCPP-Al

The synthetic procedures of Cu@TCPP-Al are briefly shown in Fig. 1a. Starting from the hydrothermal synthesis of TCPP-Al in Fig. S1a, Cu@TCPP-Al was further obtained by a post-treatment step. The X-ray diffraction (XRD) pattern of Cu@TCPP-Al matches well with that of TCPP-Al (Fig. S1b and c), with absence of characteristic peaks assigned to Cu compounds, signifying the highly dispersed status of Cu species. The field emission scanning electron microscope (FETEM) images show that the microstructure of Cu@TCPP-Al is in close proximity to that of TCPP-Al, both of which are characterized by spindle-like shape with a length of about 2 μm and a width of 500 nm (Fig. 1b and c). The combined results confirm that the introduction of Cu species did not alter the pristine crystal structure or morphology of TCPP-Al. Elemental mapping reveals the evenly distribution of all the constituent elements (C, N, O, Al and Cu) in Cu@TCPP-Al (Fig. 1d). We further confirmed the atomic dispersion of Cu species in the TCPP-Al substrate, as clearly indicated by the high-density scattered bright spots (green circles) in the HAADF-STEM image (Fig. 1e), with no identifiable Cu nanoparticles or clusters [8]. Note that these spots cannot be attributed to other elements involved in Cu@TCPP-Al (*e.g.*, Al), due to their much smaller atomic number than that of Cu. Additionally, the intensity profile (Fig. 1f) and the 3D contour map (Fig. 1g) of the selected regions also point to the fact that the high-density bright spots are dispersed separately at the atomic level. Taking together, these results collectively suggest that Cu species are highly dispersed at the atomic level in TCPP-Al. It is worth mentioning that the mass fraction of Cu species in Cu@TCPP-Al was determined to be 11.96 % (Table S1) according to the results of inductively coupled plasma-atomic emission spectrometry (ICP-AES) which is nearly identical to the theoretical value (11.30 %) obtained by DFT calculation [21]. Hence, we propose that Cu species are anchored in each TCPP ligand motif in the Cu@TCPP-Al. This lays a foundation for investigating the charge separation behavior before and after the introduction of Cu species at the porphyrin ligand inside the Cu@TCPP-Al.

The coordination environment and chemical state of Cu species inside Cu@TCPP-Al samples were analyzed using XANES and EXAFS. The Cu K-edge XANES results in Fig. 1h suggest that the valence state of Cu species in Cu@TCPP-Al is between 0 and + 2, as indicated by the position of the rising edge between Cu foil and CuO [40–42]. Additionally, the Fourier-transformed (FT)-EXAFS curve of Cu@TCPP-Al (Fig. 1i) reveals a representative peak centered at 1.52 Å, ascribed to the Cu–N

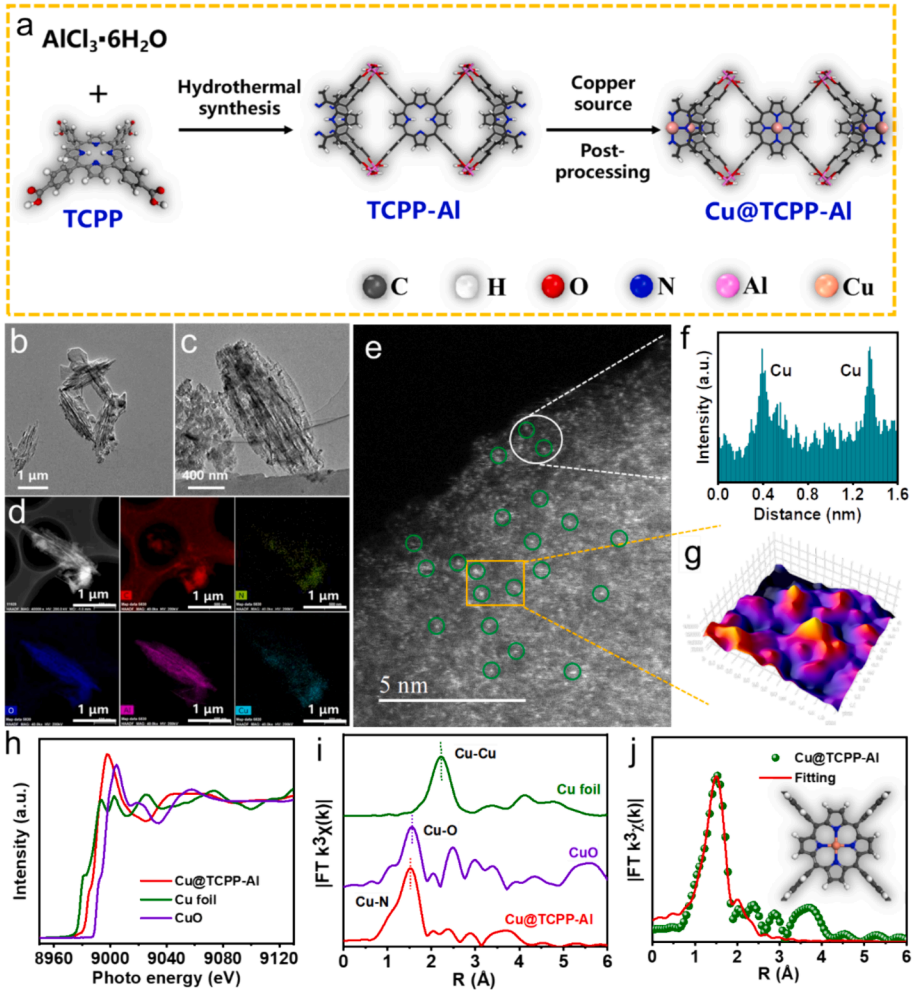

Fig. 1. Schematic diagram of the synthesis of TCPP-Al and Cu@TCPP-Al (a); FETEM images of TCPP-Al (b) and Cu@TCPP-Al (c); X-ray energy dispersive images of Cu@TCPP-Al (d); HAADF-STEM image of Cu@TCPP-Al (e), Line-scanning intensity profile along the direction of the two bright spots in the white circle area (f); Atom-overlapping Gaussian-function-fitting 3D contour map of the yellow rectangle region (g); Cu K-edge XANES spectra (h) and FT-EXAFS (i) of Cu@TCPP-Al and the reference Cu foil; FT-EXAFS fitting curve of Cu@TCPP-Al, the inset is the structural model (j).

scattering interaction [43]. The Cu–N coordination in Cu@TCPP-Al is also identified by infrared (IR) spectrum at 1000 cm^{-1}, without signals assigned to Cu–O vibration (Fig. S2) [44–46]. It is evident that these Cu ions are coordinated with pyrrolic N, which is the sole N source in the TCPP ligand [47]. Subsequently, elaborate simulations were conducted based on a structure model comprising Cu metallized porphyrin with a standard Cu-N_4 configuration. The local structure surrounding the Cu ion in Cu@TCPP-Al aligns well with the established Cu-TCPP model (Table S2), as supported by the fitted results of the major peak corresponding to the Cu–N coordination bond in R space (Fig. 1j), consistent with the FT-EXAFS result. These findings collectively confirm that the introduced Cu ions exhibit saturated coordination with pyrrolic-N (Cu-N_4) in the Cu@TCPP-Al, providing insight into its structural composition and configuration.

3.2. Photocatalytic performance and reactive oxygen species

As a model pollutant widely distributed in water bodies, ciprofloxacin (CIP) poses serious threat to human health and ecological safety. Here, we investigated the impact of anchoring Cu ions on the photocatalytic efficacy of TCPP-Al for the degradation of ciprofloxacin (CIP), employing a peroxydisulfate (PDS) activation process. Adsorption experiments under dark condition unveiled a gradual plateau in the adsorption of the target pollutant CIP by Cu@TCPP-Al after 10 min, with a final adsorption percentage of approximately 21 % (Fig. 2a, purple). Comparatively, the control group (bare PDS) contributed marginally to the degradation efficiency (5.2 %) for CIP (Fig. 2a, black), due to the weak self-decomposition ability of PDS under visible light [9,48]. Within the Cu@TCPP-Al/PDS system, the degradation rate of CIP reached 35 % within 70 min (Fig. 2a, orange). This enhancement can be attributed to the introduced semi-oxidized Cu ion, which facilitated a small portion of PDS activation but displayed limited catalytic activity, due to the absence of a driving force for valence cycling. Similarly, the Cu@TCPP-Al/Vis system only achieved 34 % degradation of CIP (Fig. 2a, blue), owing to the limited oxidizing capacity of the photogenerated holes. Moreover, it can be speculated that the generated holes are able to partially oxidize CIP and thus provide electrons to the system by comparing the degradation rates of CIP before and after illumination. The TCPP-Al/PDS/Vis system demonstrated a rather low degradation rate of 8.9 % after 70 min (Fig. 2a, green). In stark contrast, the Cu@TCPP-Al/PDS/Vis system achieved nearly 100 % degradation efficiency (Fig. 2a, red). The calculated pseudo-first-order kinetic constant (k) for CIP degradation in the Cu@TCPP-Al/PDS/Vis system was 2.90 h^{-1} (Fig. 2b), which was approximately 44 times higher than that of the TCPP-Al/PDS/Vis system (0.066 h^{-1}). Clearly, the introduction of Cu ions markedly enhanced the photocatalytic performance of TCPP-Al in PDS activation. Besides, Cu@TCPP-Al outperformed most state-of-the-art photocatalysts except for BM-5 due to its limited number of active sites, suggesting potential for further improvement in the future (Table S3).

The dominant ROS in the Cu@TCPP-Al/PDS/Vis system was then identified by radical quenching experiments and EPR spectra. As displayed in Fig. 2c, the removal efficiency of CIP decreases substantially from 98 % to 7 % or 3 % (within 60 min) upon the addition of methanol

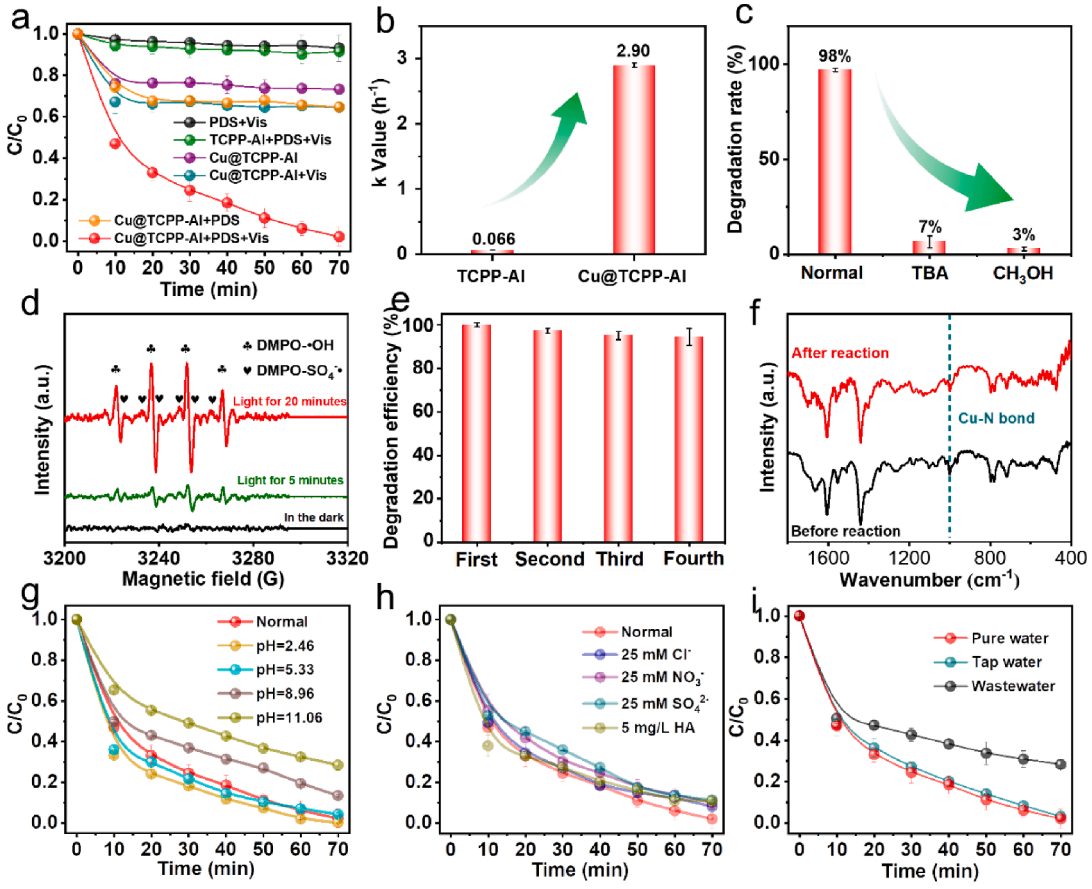

Fig. 2. CIP degradation profiles of the photocatalysts at 25 ± 2 °C under different conditions, the initial concentrations of photocatalysts, CIP and PDS were 80 mg/L, 10 mg/L and 1 mmol/L, respectively (a); Kinetics constants of CIP degradation over the TCPP-Al/PDS/Vis and Cu@TCPP-Al/PDS/Vis systems (b); Radical quenching experiment (c) and trapped radical signal using EPR (d) in Cu@TCPP-Al/PDS/Vis systems, the concentration of quencher was 200 mM; Cycling test of CIP elimination over Cu@TCPP-Al (e); IR spectra of Cu@TCPP-Al before and after reaction (f). Performance for CIP degradation in Cu@TCPP-Al/PDS/Vis systems under different pH (g), anionic (h), and aqueous matrix conditions (i).

or *tert*-butanol to the system, respectively. Methanol and *tert*-butanol serve as quenchers for $^{\bullet}OH$ and $SO_4^{\bullet-}$, respectively [48–50]. We believe that $^{\bullet}OH$ in the system is mainly generated by the reaction between H_2O and $SO_4^{\bullet-}$ generated by PDS activation (Eq. (5), consistent with most literature reports [2,51]. Also, no detectable ROS signal was observed in TCPP-Al/PDS/Vis system (Fig. S3), highlighting that the significant increase in CIP degradation efficiency is due in large part to the boosted generation of free radicals enabled by Cu ions anchoring in TCPP-Al. Comparatively, EPR captured the gradually intensified signals of DMPO-$^{\bullet}OH$ and DMPO- $SO_4^{\bullet-}$ adducts (Fig. 2d) with prolonged irradiation time, further supporting that $^{\bullet}OH$ and $SO_4^{\bullet-}$ are the major ROS for CIP degradation in the system.

The reusability and stability of Cu@TCPP-Al were further investigated. As shown in Fig. 2e, the degradation efficiency of CIP in the Cu@TCPP-Al/PDS/Vis system maintains high up to 94 % after four consecutive degradation experiments, indicating the excellent reusability of Cu@TCPP-Al photocatalyst [52,53]. On the other hand, the chemical bonds and functional groups of Cu@TCPP-Al remained intact after the reaction (Fig. 2f and Fig. S4). The XRD results reveal that the crystalline structure of the samples did not change considerably compared to the freshly prepared Cu@TCPP-Al (Fig. S5), in agreement with the results of TEM (Fig. S6). We further monitored the pH change during the reaction and found that the pH value dropped rapidly to 2.85 at the initial stage of the reaction and then remained essentially unchanged (Fig. S7), which was mainly attributed to the hydrolysis of PDS (Eq. (5) and (6) that acidified the solution. Nevertheless, the ICP-AES analyses show that the leaching amounts of Al and Cu in Cu@TCPP-Al/PDS/Vis system were as low as 0.023 mg/L (loss ratio: 0.35 %) and 0.28 mg/L (loss ratio: 2.39 %) (Table S4), respectively [54]. These results demonstrate the excellent stability of Cu@TCPP-Al.

$$H_2O + SO_4^{\bullet-} \rightarrow \bullet OH + SO_4^{2-} + H^+ \quad (5)$$

$$H_2O + S_2O_8^{2-} \rightarrow H^+ + SO_4^{2-} + O_2 \quad (6)$$

Next, we carefully evaluated the potential of the catalyst to treat practical water pollutants by evaluating the performance of the Cu@TCPP-Al/PDS/Vis system under different water matrix conditions. As shown in the Fig. 2g, the degradation efficiency of the system did not change significantly under acidic condition, which experienced slight decrease with increasing pH, due in large part to the inhibited ROS activity under alkaline environment[51,55,56]. Nevertheless, more than 71 % of CIP was removed even under strong alkaline condition (initial pH = 11.06). Also, the interfering ions (anions) and humic acids that are widely existed in complex water bodies, were found to exert minimal impact on the degradation efficiency towards CIP (Fig. 2h) [57,58]. We further evaluated the application potential of the Cu@TCPP-Al/PDS/Vis catalytic system using two practical water samples, with their common parameters listed in Table S5. The degradation efficiency of CIP

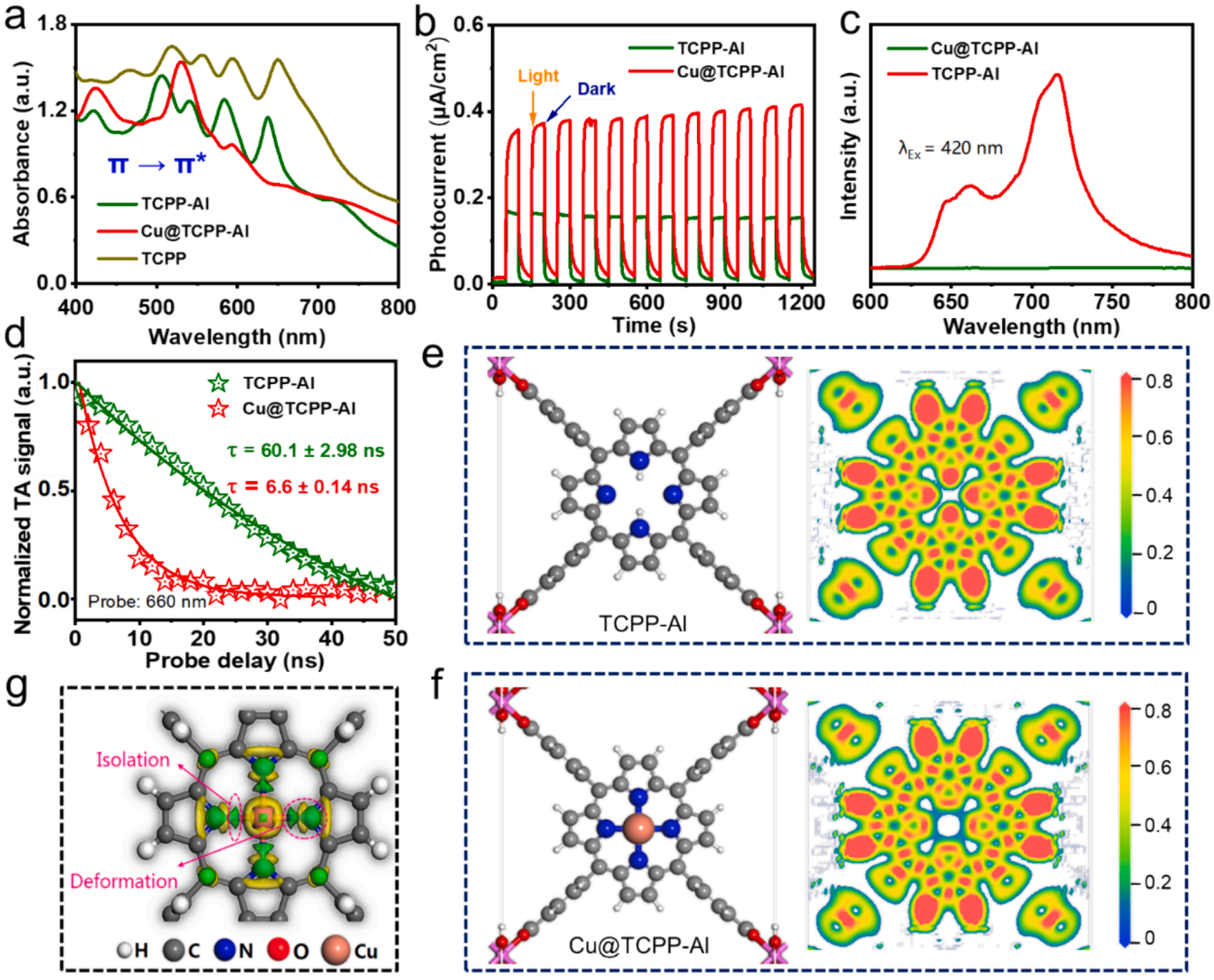

Fig. 3. UV–vis diffuse reflectance absorption spectra of the photocatalysts (a); Transient photocurrent response curves (b) and PL spectra (c) of TCPP-Al and Cu@TCPP-Al; NTA kinetics fitting of TCPP-Al and Cu@TCPP-Al using single exponential model (d); Schematic diagram of electron localization function for TCPP-Al (e) and Cu@TCPP-Al (f); distribution of charge density differences in Cu@TCPP-Al (g), where green and the yellow area represent the consumption and accumulation of charge, respectively.

remained unchanged in tap water compared to that of pure water, but it decreased in wastewater. This may be due to the coexisting organic pollutants in the wastewater consuming part of the generated ROS. Nevertheless, the Cu@TCPP-Al/PDS/Vis system was capable of degrading about 72 % of CIP within 70 min. The combined results from the degradation experiments indicate the encouraging performance of the catalyst for antibiotic removal in real wastewater.

3.3. Optical properties of Cu@TCPP-Al

The optical properties of Cu@TCPP-Al were extensively studied to reveal the potential changes after the introduction of Cu ions. As shown in Fig. 3a, the intrinsic planar π-conjugated structure of TCPP molecule exhibited a series of absorption peaks within 400–800 nm, which also held true for TCPP-Al with similar absorption profiles [17,18]. The LCCT process, as expected, did not occur in TCPP-Al, since the quadruple peaks of TCPP-Al in the 500–700 nm region (Q bands) are not red-shifted compared to those of TCPP molecule (Fig. 3a) [13,17,25]. Additionally, there were no matching energy levels of molecular orbitals (no overlap) between the $Al(OH)O_4$ cluster and TCPP ligands(Fig. S8), suggesting the absence of LCCT in TCPP-Al under light condition, in line with the findings of UV–Vis diffuse absorption spectra [59]. Comparatively, the stronger absorption peak centered at 420 nm in the UV–vis spectrum of Cu@TCPP-Al (Fig. 3a) suggests more efficient $\pi \rightarrow \pi^*$ transition when Cu ions were introduced, relative to that of bare TCPP-Al [60,61]. Another evident change is the single peak at around 530 nm in Cu@TCPP-Al, this also points to the activated $\pi \rightarrow \pi^*$ transition stemming from the rectified π orbitals, due to the delocalization of long-pair electrons from N atoms after anchoring Cu ions [17].

Given the pivotal role of the energy band structure in photocatalytic performance, we systematically evaluated the effect of Cu ions doping on the energy band structure of TCPP-Al. Using the Tauc method [62], the band gaps (E_g) of TCPP-Al and Cu@TCPP-Al were determined to be 1.6 and 1.7 eV (Figs. S9a and b), respectively. The Mott-Schottky results confirm that both TCPP-Al and Cu@TCPP-Al are n-type semiconductors, with flat-band potentials (E_{FB}) at −0.57 and −0.46 V *vs.* Ag/AgCl, (i.e., −0.373 and −0.263 V *vs.* NHE, pH = 6.8), respectively (Figs. S9c and d). Since the conduction band potential (E_{CB}) of n-type semiconductors is around 0.3 V lower than E_{FB}, the E_{CB} of TCPP-Al and Cu@TCPP-Al were −0.673 and −0.563 V *vs.* NHE, respectively [59]. Accordingly, the E_{CB}/E_{VB} (valence band potential) positions of TCPP-Al and Cu@TCPP-Al were calculated (Eq. (7) to be −0.67 V/0.93 V and −0.56 V/1.14 V *vs.* NHE (Fig. S10), respectively.

$$Eg = E_{VB} - E_{CB} \quad (7)$$

In comparison to TCPP-Al, such slight variations in the band gaps and electronic band edges after introduction of Cu ions would not significantly affect the photocatalytic performance [21]. Note that the E_{VB} positions of both TCPP-Al and Cu@TCPP-Al are lower than E_{ox} ($H_2O/^{\cdot}OH$ = 2.40 V), implying that the photogenerated holes are thermodynamically unfavored to produce $^{\cdot}OH$ via H_2O oxidation. Consequently, it is inferred that the generation of the radicals in the Cu@TCPP-Al/PDS/Vis system should be attributed to the PDS activation by photogenerated electrons.

3.4. Mechanisms for enhanced CIP degradation over Cu@TCPP-Al

The distinct electron transition in Cu@TCPP-Al can potentially lead to improved charge separation efficiency at TCPP ligand, which in turn substantially enhanced the photocatalytic performance after introducing Cu ions. After photoexcitation by visible light, the photocurrent density in Cu@TCPP-Al is noticeably higher than that in TCPP-Al, as indicated by the transient photocurrent response curves (Fig. 3b). This demonstrates that introducing Cu ions facilitates the charge transfer at the TCPP ligand inside TCPP-Al. The photoluminescence (PL) intensity of TCPP-Al is at 10^5 level (Fig. 3c), signifying the strong radiative recombination of electrons and holes [19]. Comparatively, Cu@TCPP-Al exhibits no detectable PL signal, providing solid evidence that the introduced Cu ions effectively suppress the photogenerated carrier recombination at TCPP ligand. Additionally, the kinetic behavior of photogenerated carriers were studied quantitatively by nanosecond transient absorption (NTA) spectroscopy to support the PL emission results. Specifically, the kinetic decay of the signal was recorded to obtain the lifetimes (Eq. (3), where the detection wavelength was set as 660 nm or 720 nm with reference to the PL spectra. Typically, the decay lifetime is positively correlated with the duration of the intermediate state, where photogenerated electrons cannot participate in the reaction because of confinement [8]. As shown in Fig. 3d and S11, the ineffective electron transition process within TCPP ligands eventually results in a lifetime of up to 60.1 ns (53.7 ns for 720 nm) for TCPP-Al. In contrast, Cu@TCPP-Al presents an ultrashort lifetime of only 6.6 ns (6.4 ns for 720 nm). These findings clearly demonstrate that the anchoring of Cu ions could considerably intensify the charge separation, benefiting from the activation of intrinsic electron transitions in TCPP-Al.

The origin of the dramatically intensified electron transitions after Cu ion modification was further explored by theoretical calculations. The electron localization function simulation results show that the π-electron cloud around the pyrrolic N at the center of the ligand TCPP in TCPP-Al exhibits a distinct localization feature (Fig. 3e), which is ascribed to the inherent planar π-conjugated effect [63,64]. Previous reports suggested that the localized electrons are less likely to delocalize from the conjugated system after excitation, due to the disordered and random in-plane migration [10,26]. This significantly raises the likelihood that photogenerated electrons and holes will recombine, leading to ineffective charge separation processes. In contrast, the localization degree in Cu@TCPP-Al is greatly reduced (Fig. 3f), manifesting that the introduction of Cu ions substantially facilitates delocalization. The differential charge density maps reveal that Cu ions induce a deformation and even partial isolation of the π-electrons cloud around pyrrolic N (Fig. 3g). The partial density of states also shows that the π-electrons cloud density in the N 1 s orbital decreases obviously after introducing Cu ions (Fig. S12a). Additionally, the high-resolution N 1 s XPS spectra signify that the original C = N and N–H covalent bonds are dominated by N-Cu coordination bonds after introducing Cu ions (Fig. S12b) [10,65]. These findings further indicate that some of the π-electrons around pyrrolic N are isolated from the planar π-conjugated system, that is, the delocalization starts to play pivotal role to excite the π-electrons for efficient charge separation [64,66]. Hence, the DFT calculations suggest that the π-electron localization in the planar π-conjugated system is primarily responsible for the feeble electric transition at TCPP ligands. In comparison, the introduction of Cu ions enhances efficiency in terms of delocalizing partial π-electrons for improved electron transition at TCPP ligands. The strengthened delocalization effect is also identified in other widely explored transition-metal species systems, as indicated by the calculation results of electron localization function (Fig. S13). Among these, Cu ions feature the strongest binding ability to TCPP-Al (Fig. S14), keeping consistent with the aforementioned stability of Cu@TCPP-Al in photocatalytic performance evaluation.

Finally, the relationship between the improved electron transitions and PDS activation was elucidated through analyzing the behavior of the delocalized π-electrons with the support of in-situ EPR data. The weak spin signal centered at $g = 1.996$ in TCPP-Al under dark condition arises from the unpaired electrons in TCPP ligand (Fig. 4a) [20,67]. No discernible change was detected after 2 mins of illumination, which is indicative of the localized state of the π-electrons [10,26]. For Cu@TCPP-Al, an obvious spin signal assigned to Cu ion with unsaturated 3d orbital was observed at $g = 2.045$ under dark condition (Fig. 4a) [68,69]. The gradually attenuated signal intensity with prolonging irradiation time should be ascribed to the isolated electrons around pyrrolic N leaping into the Cu 3d orbital. Consequently, the in-situ EPR results establish that the delocalized π-electrons around pyrrolic N in

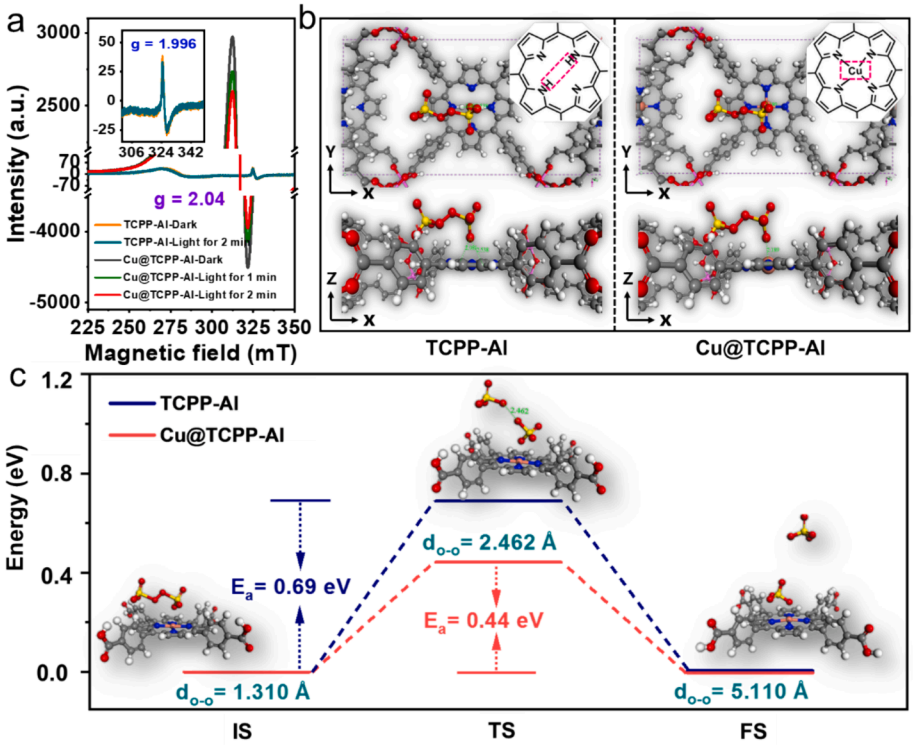

Fig. 4. In-situ EPR spectra of TCPP-Al and Cu@TCPP-Al (a); Geometrically optimized PDS adsorption model over TCPP-Al and Cu@TCPP-Al (b); Simplified diagram of energy barrier distribution for O-O bond cleavage reaction in TCPP-Al and Cu@TCPP-Al upon PDS activation (c).

Cu@TCPP-Al after visible light irradiation are easily excited and transferred to Cu 3d orbital, forming electron-rich centers that reduce the reaction energy barrier [10,12]. Besides, the adsorption and activation behaviors of PDS molecules in TCPP-Al before and after Cu ions doping were studied by DFT calculations. Compared with TCPP-Al (−5.70 eV), PDS has a better affinity to Cu ion with a more negative adsorption energy (−5.98 eV) in Cu@TCPP-Al, which is more conducive to the subsequent activation process (Fig. 4b) [48]. As expected, the energy barrier for the rate-limiting step in the PDS activation process, i.e., the O-O bond cleavage pathway, is reduced from 0.69 to 0.44 eV after doping Cu ions, as shown in Fig. 4c.

To sum up, the introduced Cu ions afford efficient electron transitions inside TCPP-Al upon illumination by delocalizing the π-electrons around pyrrolic N within TCPP ligands. Along with this, the delocalized π-electrons are transferred to the Cu ions site for efficient activation of PDS to generate $^{\bullet}OH$ and $SO_4^{\bullet-}$, which ultimately contribute to the effective degradation of CIP (Fig. 5).

4. Conclusion

This work demonstrates, for the first time, that activated π → π* transition induced by Cu ions over PMOFs can enhance photocatalytic

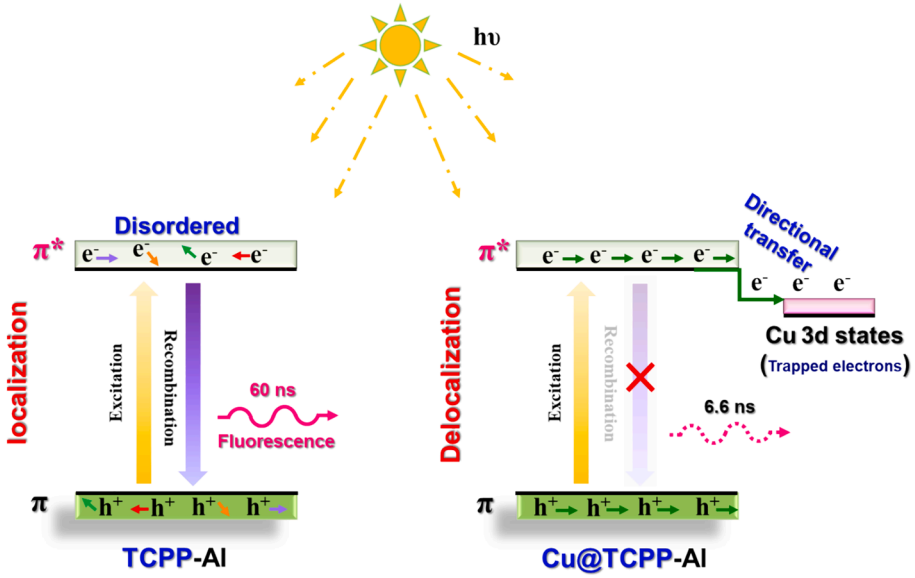

Fig. 5. Schematic diagram of π → π* transition at the ligand before and after doping of Cu ions.

activation of PDS, leading to efficient pollutant degradation. The developed Cu@TCPP-Al photocatalyst achieves approximately a 44-fold higher kinetic constant in CIP degradation under visible light irradiation. Electron localization in the π-conjugated structure constitutes the primary reason for the ineffective $\pi \rightarrow \pi^*$ transition at the PMOF ligands. However, the introduction of Cu ions into the conjugated framework enables efficient electron transitions by partially delocalizing the π-electrons. Further results indicate that the delocalized π-electrons can migrate to Cu sites and form electron-rich centers under visible light irradiation. This process activates the adsorbed PDS molecules are activated by lowering the energy barrier for O-O bond cleavage, generating $^{\bullet}OH$ and $SO_4^{\bullet-}$ as ROS for efficient catalytic degradation. The enhanced electron transitions within the ligand porphyrin via delocalization can be rationally extended to other common transition-metal systems. This study provides a molecule-level insight into the charge separation process inside PMOFs, promising rational design for improved decontamination performance via advanced oxidation process.

CRediT authorship contribution statement

Wen-Qiang Li: Writing – review & editing, Writing – original draft, Visualization, Validation, Resources, Methodology, Formal analysis, Data curation, Conceptualization. **Oleksandr Savateev:** Validation, Methodology, Investigation, Formal analysis, Data curation. **Yuan-Ming Li:** Visualization, Validation, Methodology, Formal analysis. **Jian-Kang Zheng:** Visualization, Validation, Methodology, Formal analysis. **Yi-Xuan Wang:** Visualization, Methodology, Investigation, Formal analysis. **Nannan Hou:** Writing – review & editing, Writing – original draft, Validation, Supervision, Methodology, Funding acquisition, Formal analysis, Conceptualization. **Xiao-Cheng Liu:** Visualization, Validation, Resources, Formal analysis. **Rong-Rong Ding:** Resources, Formal analysis, Data curation. **Xiao-Guo Zhou:** Visualization, Resources. **Yang Wang:** Writing – review & editing, Writing – original draft, Validation, Supervision, Resources, Methodology, Investigation, Formal analysis, Data curation, Conceptualization. **Xian-Yang Shi:** Writing – review & editing, Writing – original draft, Validation, Supervision, Formal analysis, Data curation, Conceptualization. **Yang Mu:** Writing – review & editing, Writing – original draft, Validation, Supervision, Resources, Methodology, Investigation, Formal analysis, Data curation, Conceptualization.

Declaration of competing interest

The authors declare that they have no known competing financial interests or personal relationships that could have appeared to influence the work reported in this paper.

Data availability

Data will be made available on request.

Acknowledgements

We acknowledge the financial support from the National Natural Science Foundation of China (52300021, 52025101, U23A20676, 52200073 and 51878637). Dr. Yang Wang thanks the Alexander von Humboldt Foundation for a postdoctoral fellowship.

Appendix A. Supplementary data

Supplementary data to this article can be found online at https://doi.org/10.1016/j.cej.2024.151802.

References

[1] Z.Y. Guo, C.X. Li, M. Gao, X. Han, Y.J. Zhang, W.J. Zhang, W.W. Li, Mn-O covalency governs the intrinsic activity of Co-Mn spinel oxides for boosted peroxymonosulfate activation, Angew. Chem. Int. Ed. 60 (2021) 274–280.
[2] L.Y. Wu, Z. Sun, Y.F. Zhen, S.S. Zhu, C. Yang, J. Lu, Y. Tian, D. Zhong, J. Ma, Oxygen vacancy-induced nonradical degradation of organics: critical trigger of oxygen (O2) in the Fe-Co LDH/peroxymonosulfate system, Environ. Sci. Technol. 55 (2021) 15400–15411.
[3] H.Y. Dong, Q.X.L.S. Lian, Y. Li, S.C. Wang, C. Li, X.H. Guan, Degradation of organic contaminants in the Fe(II)/peroxymonosulfate process under acidic conditions: The overlooked rapid oxidation stage, Environ. Sci. Technol. 55 (2021) 15390–15399.
[4] C. Chen, Z. Wu, Z. Hua, K. Guo, Y. Zhou, D. Wang, B. Xia, J. Fang, Mechanistic and kinetic understanding of micropollutant degradation by the UV/NH_2Cl process in simulated drinking water, Water Res. 204 (2021) 117569.
[5] T.K. Lau, W. Chu, N.J.D. Graham, The aqueous degradation of butylated hydroxyanisole by UV/$S_2O_8^{2-}$: Study of reaction mechanisms via dimerization and mineralization, Environ. Sci. Technol. 41 (2007) 613–619.
[6] F. Chen, G.X. Huang, F.B. Yao, Q. Yang, Y.M. Zheng, Q.B. Zhao, H.Q. Yu, Catalytic degradation of ciprofloxacin by a visible-light-assisted peroxymonosulfate activation system: Performance and mechanism, Water Res 173 (2020).
[7] X. Fang, Q. Shang, Y. Wang, L. Jiao, T. Yao, Y. Li, Q. Zhang, Y. Luo, H.L. Jiang, Single Pt atoms confined into a metal-organic framework for efficient photocatalysis, Adv Mater. 30 (2018) 1705112.
[8] Y. Wen, A.N. Rentería-Gómez, G.S. Day, M.F. Smith, T.H. Yan, R.O.K. Ozdemir, O. Gutierrez, V.K. Sharma, X. Ma, H.C. Zhou, Integrated photocatalytic reduction and oxidation of perfluorooctanoic acid by metal-organic frameworks: key insights into the degradation mechanisms, J. Am. Chem. Soc. 144 (2022) 11840–11850.
[9] Y. Gao, S. Li, Y. Li, L. Yao, H. Zhang, Accelerated photocatalytic degradation of organic pollutant over metal-organic framework MIL-53 (Fe) under visible LED light mediated by persulfate, Appl. Catal. B-Environ. 202 (2017) 165–174.
[10] L. Su, P. Wang, X. Ma, J. Wang, S. Zhan, Regulating local electron density of iron single sites by introducing nitrogen vacancies for efficient photo-Fenton process, Angew. Chem. Int. Ed. 60 (2021) 21261–21266.
[11] J. Yang, M. Zhu, D.D. Dionysiou, What is the role of light in persulfate-based advanced oxidation for water treatment? Water Res. 189 (2021) 116627.
[12] P. Zhao, Y. Jiang, Z. Tang, Y. Li, B. Sun, Y. Wu, J. Wu, Y. Liu, W. Bu, Constructing electron levers in perovskite nanocrystals to regulate the local electron density for intensive chemodynamic therapy, Angew. Chem. Int. Ed. 60 (2021) 8905–8912.
[13] T. Zhang, W. Lin, Metal-organic frameworks for artificial photosynthesis and photocatalysis, Chem Soc Rev 43 (2014) 5982–5993.
[14] M.A. Nasalevich, M. van der Veen, F. Kapteijn, J. Gascon, Metal-organic frameworks as heterogeneous photocatalysts: advantages and challenges, CrystEngComm 16 (2014) 4919–4926.
[15] Y. Chen, T. Hoang, S. Ma, Biomimetic catalysis of a porous iron-based metal-metalloporphyrin framework, Inorg. Chem. 51 (2012) 12600–12602.
[16] D. Feng, Z.Y. Gu, J.R. Li, H.L. Jiang, Z. Wei, H.C. Zhou, Zirconium-metalloporphyrin PCN-222: mesoporous metal–organic frameworks with ultrahigh stability as biomimetic catalysts, Angew. Chem. Int. Ed. 51 (2012) 10307–10310.
[17] J. Chen, Y. Zhu, S. Kaskel, Porphyrin-based metal-organic frameworks for biomedical applications, Angew. Chem. Int. Ed. 60 (2021) 5010–5035.
[18] W.Y. Gao, M. Chrzanowski, S. Ma, Metal-metalloporphyrin frameworks: a resurging class of functional materials, Chem. Soc. Rev. 43 (2014) 5841–5866.
[19] Z. Zhang, Y. Zhu, X. Chen, H. Zhang, J. Wang, A full-spectrum metal-free porphyrin supramolecular photocatalyst for dual functions of highly efficient hydrogen and oxygen evolution, Adv. Mater. 31 (2019) 1806626.
[20] C. Zou, C.D. Wu, Functional porphyrinic metal-organic frameworks: crystal engineering and applications, Dalton Trans. 41 (2012) 3879–3888.
[21] A. Aziz, A.R. Ruiz-Salvador, N.C. Hernández, S. Calero, S. Hamad, R. Grau-Crespo, Porphyrin-based metal-organic frameworks for solar fuel synthesis photocatalysis: band gap tuning via iron substitutions, J. Mater. Chem. A 5 (2017) 11894–11904.
[22] W.Q. Li, Y.X. Wang, J.Q. Chen, N.N. Hou, Y.M. Li, X.C. Liu, R.R. Ding, G.N. Zhou, Q. Li, X.G. Zhou, Boosting photo-Fenton process enabled by ligand-to-cluster charge transfer excitations in iron-based metal organic framework, Appl. Catal. B-Environ. 302 (2022) 120882.
[23] N. Sharma, A.K. Dey, R.Y. Sathe, A. Kumar, V. Krishnan, T.D. Kumar, C. Nagaraja, Highly efficient visible-light-driven reduction of Cr(VI) from water by porphyrin-based metal-organic frameworks: effect of band gap engineering on the photocatalytic activity, Catal. Sci. Technol. 10 (2020) 7724–7733.
[24] C.Y. Xu, H. Liu, D. Li, J.H. Su, H.L. Jiang, Direct evidence of charge separation in a metal-organic framework: efficient and selective photocatalytic oxidative coupling of amines via charge and energy transfer, Chem. Sci. 9 (2018) 3152–3158.
[25] C.H. Hendon, D. Tiana, M. Fontecave, C.M. Sanchez, L. D'arras, C. Sassoye, L. Rozes, C. Mellot-Draznieks, A. Walsh, Engineering the optical response of the titanium-MIL-125 metal-organic framework through ligand functionalization, J. Am. Chem. Soc. 135 (2013) 10942–10945.
[26] S. Cao, H. Li, T. Tong, H.C. Chen, A. Yu, J. Yu, H.M. Chen, Single-atom engineering of directional charge transfer channels and active sites for photocatalytic hydrogen evolution, Adv. Funct. Mater. 28 (2018) 1802169.
[27] L. Chen, J.T. Ren, Z.Y. Yuan, Atomic heterojunction-induced electron interaction in P-doped g-C_3N_4 nanosheets supported V-based nanocomposites for enhanced oxidative desulfurization, Chem. Eng. J. 387 (2020) 124164.
[28] P. Xia, B. Cheng, J. Jiang, H. Tang, Localized π-conjugated structure and EPR investigation of g-C_3N_4 photocatalyst, Appl. Surf. Sci. 487 (2019) 335–342.
[29] T. Xiong, W. Cen, Y. Zhang, F. Dong, Bridging the g-C_3N_4 interlayers for enhanced photocatalysis, ACS Catal. 6 (2016) 2462–2472.

[30] C.A. Caputo, M.A. Gross, V.W. Lau, C. Cavazza, B.V. Lotsch, E. Reisner, Photocatalytic hydrogen production using polymeric carbon nitride with a hydrogenase and a bioinspired synthetic Ni catalyst, Angew. Chem. Int. Ed. 53 (2014) 11538–11542.
[31] S.W. Cao, X.F. Liu, Y.P. Yuan, Z.Y. Zhang, J. Fang, S.C.J. Loo, J. Barber, T.C. Sum, C. Xue, Artificial photosynthetic hydrogen evolution over gC_3N_4 nanosheets coupled with cobaloxime, Phys. Chem. Chem. Phys. 15 (2013) 18363–18366.
[32] Y. Liu, Y. Yang, Q. Sun, Z. Wang, B. Huang, Y. Dai, X. Qin, X. Zhang, Chemical adsorption enhanced CO_2 capture and photoreduction over a copper porphyrin based metal organic framework, ACS Appl. Mater. Interfaces 5 (2013) 7654–7658.
[33] Z. Zhang, Y. Zhu, X. Chen, H. Zhang, J. Wang, A full-spectrum metal-free porphyrin supramolecular photocatalyst for dual functions of highly efficient hydrogen and oxygen evolution, Adv Mater. 31 (2019) e1806626.
[34] A. Fateeva, P.A. Chater, C.P. Ireland, A.A. Tahir, Y.Z. Khimyak, P.V. Wiper, J. R. Darwent, M.J. Rosseinsky, A water-stable porphyrin-based metal-organic framework active for visible-light photocatalysis, Angew. Chem. Int. Ed. 51 (2012) 7440–7444.
[35] D.S. Biovia, Materials Studio, R2, Dassault Systèmes BIOVIA, San Diego, 2017.
[36] S.J. Clark, M.D. Segall, C.J. Pickard, P.J. Hasnip, M.I. Probert, K. Refson, M. C. Payne, First principles methods using CASTEP, Z Kristallogr Cryst Mater 220 (2005) 567–570.
[37] J. Nisar, C. Århammar, E. Jämstorp, R. Ahuja, Optical gap and native point defects in kaolinite studied by the GGA-PBE, HSE functional, and GW approaches, Phys. Rev. B 84 (2011) 075120.
[38] B. Delley, From molecules to solids with the DMol 3 approach, The, J. Chem. Phys. 113 (2000) 7756–7764.
[39] S. Hamad, N.C. Hernandez, A. Aziz, A.R. Ruiz-Salvador, S. Calero, R. Grau-Crespo, Electronic structure of porphyrin-based metal-organic frameworks and their suitability for solar fuel production photocatalysis, J. Mater. Chem. A 3 (2015) 23458–23465.
[40] X. Bai, X. Zhao, Y. Zhang, C. Ling, Y. Zhou, J. Wang, Y. Liu, Dynamic stability of copper single-atom catalysts under working conditions, J. Am. Chem. Soc. 144 (2022) 17140–17148.
[41] Y. Cai, J. Fu, Y. Zhou, Y.C. Chang, Q. Min, J.J. Zhu, Y. Lin, W. Zhu, Insights on forming N, O-coordinated Cu single-atom catalysts for electrochemical reduction CO_2 to methane, Nat. Commun. 12 (2021) 586.
[42] X. Lu, S. Gao, H. Lin, L. Yu, Y. Han, P. Zhu, W. Bao, H. Yao, Y. Chen, J. Shi, Bioinspired copper single-atom catalysts for tumor parallel catalytic therapy, Adv. Mater. 32 (2020) 2002246.
[43] J. Li, M. Li, N. An, S. Zhang, Q. Song, Y. Yang, X. Liu, Atomically dispersed Fe atoms anchored on S and N-codoped carbon for efficient electrochemical denitrification, Proc. Natl. Acad. Sci. USA 118 (2021) e2105628118.
[44] L. Wang, P. Jin, S. Duan, H. She, J. Huang, Q. Wang, In-situ incorporation of Copper(II) porphyrin functionalized zirconium MOF and TiO2 for efficient photocatalytic CO2 reduction, Sci. Bull. 64 (2019) 926–933.
[45] S.K. Shinde, D.P. Dubal, G.S. Ghodake, P. Gomez-Romero, S. Kim, V.J. Fulari, Influence of Mn incorporation on the supercapacitive properties of hybrid CuO/Cu (OH)2 electrodes, RSC Adv. 5 (2015) 30478–30484.
[46] D. Lai, T. Liu, X. Gu, Y. Chen, J. Niu, L. Yi, W. Chen, Suspension synthesis of surfactant-free cuprous oxide quantum dots, J. Nanomater. 2015 (2015) 825021.
[47] Z. Yang, B. Chen, W. Chen, Y. Qu, F. Zhou, C. Zhao, Q. Xu, Q. Zhang, X. Duan, Y. Wu, Directly transforming copper(I) oxide bulk into isolated single-atom copper sites catalyst through gas-transport approach, Nat. Commun. 10 (2019) 1–7.
[48] C. Wang, J. Kim, V. Malgras, J. Na, J. Lin, J. You, M. Zhang, J. Li, Y. Yamauchi, Metal-organic frameworks and their derived materials: Emerging catalysts for a sulfate radicals-based advanced oxidation process in water purification, Small 15 (2019) 1900744.
[49] Z.H. Xie, C.S. He, H.Y. Zhou, L.L. Li, Y. Liu, Y. Du, W. Liu, Y. Mu, B. Lai, Effects of molecular structure on organic contaminants' degradation efficiency and dominant ROS in the advanced oxidation process with multiple ROS, Environ. Sci. Technol. 56 (2022) 8784–8795.
[50] S.R. Yang, C.S. He, Z.H. Xie, L.L. Li, Z.K. Xiong, H. Zhang, P. Zhou, F. Jiang, Y. Mu, B. Lai, Efficient activation of PAA by FeS for fast removal of pharmaceuticals: The dual role of sulfur species in regulating the reactive oxidized species, Water Res. 217 (2022) 118402.
[51] H.Y. Gao, C.H. Huang, L. Mao, B. Shao, J. Shao, Z.Y. Yan, M. Tang, B.Z. Zhu, First direct and unequivocal electron spin resonance spin-trapping evidence for pH-dependent production of hydroxyl radicals from sulfate radicals, Environ. Sci. Technol. 54 (2020) 14046–14056.
[52] S. Shang, W. Xiong, C. Yang, B. Johannessen, R. Liu, H.Y. Hsu, Q. Gu, M.K. Leung, J. Shang, Atomically dispersed iron metal site in a porphyrin-based metal-organic framework for photocatalytic nitrogen fixation, ACS Nano 15 (2021) 9670–9678.
[53] Y. Shang, X. Xu, B. Gao, S. Wang, X. Duan, Single-atom catalysis in advanced oxidation processes for environmental remediation, Chem. Soc. Rev. 50 (2021) 5281–5322.
[54] M. Ahmad, X. Quan, S. Chen, H. Yu, Tuning Lewis acidity of MIL-88B-Fe with mix-valence coordinatively unsaturated iron centers on ultrathin Ti_3C_2 nanosheets for efficient photo-Fenton reaction, Appl. Catal. B-Environ. 264 (2020) 118534.
[55] F. Rezaei, D. Vione, Effect of pH on zero valent iron performance in heterogeneous fenton and fenton-like processes: A review, Molecules 23 (2018) 3127.
[56] L. Wang, B. Li, D.D. Dionysiou, B. Chen, J. Yang, J. Li, Overlooked formation of H_2O_2 during the hydroxyl radical-scavenging process when using alcohols as scavengers, Environ. Sci. Technol. 56 (2022) 3386–3396.
[57] M. Chen, J. Yao, Y. Huang, H. Gong, W. Chu, Enhanced photocatalytic degradation of ciprofloxacin over Bi2O3/(BiO)2CO3 heterojunctions: efficiency, kinetics, pathways, mechanisms and toxicity evaluation, Chem. Eng. J. 334 (2018) 453–461.
[58] M. Feng, X. Wang, J. Chen, R. Qu, Y. Sui, L. Cizmas, Z. Wang, V.K. Sharma, Degradation of fluoroquinolone antibiotics by ferrate (VI): Effects of water constituents and oxidized products, Water Res. 103 (2016) 48–57.
[59] F. Chen, L.L. Liu, Y.J. Zhang, J.H. Wu, G.X. Huang, Q. Yang, J.J. Chen, H.Q. Yu, Enhanced full solar spectrum photocatalysis by nitrogen-doped graphene quantum dots decorated BiO_{2-x} nanosheets: Ultrafast charge transfer and molecular oxygen activation, Appl. Catal. B-Environ. 277 (2020) 119218.
[60] M. Lee, D. Lee, W. Yen, C. Yeh, Synthesis, optical and photovoltaic properties of porphyrin dyes, J MACROMOL SCI A 46 (2009) 730–737.
[61] H.D. Arbelo-López, A.D. Rodriguez-Mackenzie, E.M. Roman-Morales, T. Wymore, J. López-Garriga, Charge transfer and π to π^* transitions in the visible spectra of sulfheme met isomeric structures, J. Phys. Chem. B 122 (2018) 4947–4955.
[62] H.Q. Xu, J. Hu, D. Wang, Z. Li, Q. Zhang, Y. Luo, S.H. Yu, H.L. Jiang, Visible-light photoreduction of CO_2 in a metal-organic framework: boosting electron-hole separation via electron trap states, J. Am. Chem. Soc. 137 (2015) 13440–13443.
[63] A. Savin, R. Nesper, S. Wengert, T.F. Fässler, ELF: The electron localization function, Angew. Chem. Int. Ed. 36 (1997) 1808–1832.
[64] P. Huang, W. Liu, Z. He, C. Xiao, T. Yao, Y. Zou, C. Wang, Z. Qi, W. Tong, B. Pan, Single atom accelerates ammonia photosynthesis, Sci China Chem 61 (2018) 1187–1196.
[65] Q. Zuo, T. Liu, C. Chen, Y. Ji, X. Gong, Y. Mai, Y. Zhou, Ultrathin metal-organic framework nanosheets with ultrahigh loading of single Pt atoms for efficient visible-light-driven photocatalytic H2 evolution, Angew. Chem. Int. Ed. 58 (2019) 10198–10203.
[66] D. Balzer, I. Kassal, Even a little delocalization produces large kinetic enhancements of charge-separation efficiency in organic photovoltaics, Sci. Adv. 8 (2022) eabl9692.
[67] P. Xia, X. Pan, S. Jiang, J. Yu, B. He, P.M. Ismail, W. Bai, J. Yang, L. Yang, H. Zhang, Designing a redox heterojunction for photocatalytic "overall nitrogen fixation" under mild conditions, Adv. Mater. (2022), 2200563.
[68] Q. Lu, J. Zhang, P. Peng, G. Zhang, Z. Huang, H. Yi, J.T. Miller, A. Lei, Operando X-ray absorption and EPR evidence for a single electron redox process in copper catalysis, Chem. Sci. 6 (2015) 4851–4854.
[69] L. Wang, H. Xu, N. Jiang, Z. Wang, J. Jiang, T. Zhang, Trace cupric species triggered decomposition of peroxymonosulfate and degradation of organic pollutants: Cu(III) being the primary and selective intermediate oxidant, Environ. Sci. Technol. 54 (2020) 4686–4694.